

# In Search of Global 21-cm Signal using Artificial Neural Network in light of ARCADE 2

Vivekanand Mohapatra<sup>1\*</sup>, Johnny J<sup>1</sup>, Pravin Kumar Natwariya<sup>2,3†</sup>, Jishnu Goswami<sup>4</sup>, Alekha C. Nayak<sup>1</sup>

<sup>1</sup>Department of Physics, National Institute of Technology Meghalaya, Meghalaya 793 003, India

<sup>2</sup>Physical Research Laboratory, Theoretical Physics Division, Ahmedabad, Gujarat 380 009, India

<sup>3</sup>Department of Physics, Indian Institute of Technology, Gandhinagar, Palaj, Gujarat 382 355, India

<sup>4</sup>RIKEN Center for Computational Science, 7-1-26 Minatojima-minamimachi, Chuo-ku, Kobe, Hyogo 650 0047, Japan

Accepted XXX. Received YYY; in original form ZZZ

## ABSTRACT

Understanding the astrophysical nature of the first stars still remains an unsolved problem in cosmology. The redshifted global 21-cm signal ( $T_{21}$ ) acts as a treasure trove to probe the Cosmic Dawn era— when the intergalactic medium was mostly neutral. Many experiments, like SARAS 3, EDGES, and DARE have been proposed to probe the cosmic dawn era. However, extracting the faint cosmological signal buried inside a brighter foreground  $O(10^4)$  remains challenging. Thus we use two artificial neural networks, one for extraction of foreground, via parameter estimation with R-square ( $R^2$ ) score ( $0.8034 - 0.9984$ ), from the total sky-averaged spectrum. The other is for extraction of a global 21-cm signal in the presence of noise with  $R^2$  score ( $0.6960 - 0.9978$ ). Considering an excess radio background scenario, we constructed all possible  $T_{21}$  signals in the EDGES limit, along with the foreground signal, to train the neural networks. Here, we also explore the variation in parameter estimation due to the presence of heating of intergalactic medium by background radio radiation mediated via  $\text{Ly}\alpha$  photons from first stars, and we found that the presence and absence of this effect can change the global 21-cm signal estimation by  $\sim 33$  mK in the EDGES limit ( $\sim -0.5$  K).

**Key words:** cosmology: first stars, observations, cosmological parameters, method: data analysis

## 1 INTRODUCTION

The evolution of the Intergalactic Medium (IGM) during the Cosmic Dawn (CD) era and the Epoch of Reionization (EoR) lacks a comprehensive understanding due to the uncertainty in the known physics of the formation and evolution of the first stars and galaxies in the Universe. The Global 21-cm signal (Pritchard & Loeb (2012); Furlanetto et al. (2006)) and 21-cm power spectrum (Bharadwaj & Sethi (2001); Morales & Wyithe (2010); Morales (2005)) are the two treasure troves to probe these epochs. Many experiments have been conducted, like, SARAS (Patra et al. (2013)), SARAS 2 (Singh et al. (2017)), SARAS 3 (Singh et al. (2022)), REACH (de Lera Acedo et al. (2022)), SCI-HI (Voytek et al. (2014)), HERA (DeBoer et al. (2017)), DARE (Burns et al. (2012, 2017)) to measure these. Recently, EDGES collaboration (Bowman et al. (2018)) has reported a 21-cm signal with an absorption of  $\sim 0.5^{+0.2}_{-0.5}$  K in the redshift range  $15 - 20$ — which is twice the value predicted by the standard  $\Lambda$ CDM model of cosmology (Bowman et al. (2018)). Although SARAS 3 (Bevins et al. (2022)) have rejected the EDGES signal with a 95.3% confidence level after conducting an independent check, yet the actual shape is unknown. If future experiments confirm a trough of amplitude greater than  $\sim 0.2$  K, which is the standard value, that could lead to a completely new insight into the physics of these epochs. Following the EDGES detection, several

models have been proposed to construct all possible shapes and amplitudes of the global 21-cm signal. In the references (Barkana et al. (2018); Slatyer & Wu (2018)), the authors have considered excess cooling of IGM by Dark Matter-Baryon scattering, (Natwariya & Bhatt (2020)) have considered Primordial Magnetic Fields (PMFs) and (Bhatt et al. (2020)) DM-Baryon Scattering in presence of PMFs, (Natwariya et al. (2021); Saha & Laha (2022)) have considered energy injected due to Primordial Black Holes (PBHs) and (Natwariya & Nayak (2022)) decaying sterile neutrinos, to explain the EDGES absorption signal.

In addition to that, (Fialkov et al. (2018); Fraser et al. (2018); Feng & Holder (2018); Pospelov et al. (2018)) have considered excess-radio background radiation, which could be due to several phenomena, like stimulated emission from Bose (axion) star (Levkov et al. (2020)), radio emission from Pop III black holes (Mebane et al. (2020)), conversion of axion-photon in presence of magnetic field (Moroi et al. (2018)), and radio photon from PBHs (Mittal & Kulkarni (2022)). Recently, ARCADE 2 (Feng & Holder (2018); Fixsen et al. (2011)) and LWA1 (Dowell & Taylor (2018)) have detected an excess-radio background in the frequency range of  $3 - 10$  GHz and  $40 - 80$  MHz, respectively. ARCADE 2 detection mimics the Cosmic Microwave Background Radiation (CMBR) for a frequency  $\nu > 10$  GHz but deviated significantly otherwise. These detections have been modelled by a power law with a spectral index ( $\beta$ ) of  $-2.62 \pm 0.04$  and  $-2.58 \pm 0.05$  for ARCADE 2 and LWA1, respectively.

Detecting the 21-cm signal (mK) buried in a sea full of bright foreground radiation of the  $O(10^4)$  stronger is an observation challenge.

\* E-mail: vivekanandmohapatra@gmail.com

† E-mail: pvn.sps@gmail.com

In addition to that, the ionospheric effect, radio frequency interference (RFI), and instrument response make it a tougher job. These effects, especially ionospheric distortion and RFI, can be reduced significantly if one considers far-side Moon-based experiments like DARE (Burns et al. (2012, 2017)). One of the most common techniques adapted to remove the foreground radiation is considering it well-characterized and spectrally smooth. After removing the foreground radiation, the residual contains the global 21-cm signal having the signature of the IGM evolution.

Machine Learning (ML) techniques have been used previously by many authors to study the CD and EoR. (Shimabukuro & Semelin (2017); Schmit & Pritchard (2018)) have used artificial neural networks (ANN) for parameter extraction from the 21-cm power spectrum. In the references (Jennings et al. (2019); Hassan et al. (2019); Chardin et al. (2019); Gillet et al. (2019)), a convolutional neural network (CNN) has been used to study and extract parameters from the 21-cm maps. Other than ANN being used for parameter estimations, emulators trained with global 21-cm signals simulated results are also being used to generate model-based global 21-cm signal realisations, for example 21cmGEM (Cohen et al. (2020)), 21cmVAE (Bye et al. (2022)), and GLOBALEMU (Bevins et al. (2021)). Provided seven astrophysical free parameters, the emulator is enabled to produce global 21-cm signals in a redshift  $z = 5 - 50$  using a series of NNs, a tree classifier, and principal component analysis (Cohen et al. (2020)). The objective of these emulators is to learn the relationship between parameters and the global 21-cm signal without enforcing a physical model. However, our work focuses on parameter estimation and signal extraction using ANNs. (Choudhury et al. (2020, 2021)) have used global 21-cm signal and reionization simulations for parameter extraction using a single ANN in the presence of foreground contamination for parameter extraction from synthetic and EDGES data. Unlike previous works, we have used two trained ANNs instead of one for signal extraction. One of the ANNs is used to extract the foreground signal and the other is to predict parameters associated with IGM properties via the global 21-cm signal. First, we generate the datasets for the 21-cm signal by varying the free parameters described in section (4). Here we have generated two types of 21-cm signal datasets: one consists of the IGM heating due to the radio background mediated by  $\text{Ly}\alpha$  radiation from first stars (Venumadhav et al. (2018)), and in the second type of dataset we do not include this effect to show how the parameter estimation changes. After the generation of the datasets, we add foreground radiation and noise for training and prediction purposes.

This work is organised as follows: In section (2) briefly introduces the global 21-cm signal and excess background radiation. Section (3), the evolution of the IGM temperature and the importance of IGM heating due to the radio background mediated by  $\text{Ly}\alpha$  radiation from first stars in excess background radiation. In section (4 - 5), construction of the global 21-cm signal and foreground along with the corresponding associated parameters. In section (6), we briefly introduce the ANNs, construction of training and prediction data sets. In section (7), we estimate the IGM parameters from noisy data. Section (8) includes a summary, conclusion and outlook.

## 2 THE GLOBAL 21-CM SIGNAL

The hyperfine transition between 1S singlet ( $n_0$ ) and triplet ( $n_1$ ) states in a neutral hydrogen atom (HI) occur due to the interaction of proton and electron spin. The relative number density of neutral hydrogen in triplet and singlet states is characterized by spin

temperature ( $T_s$ )

$$\frac{n_1}{n_0} = \frac{g_1}{g_0} e^{-2\pi\nu_{21}/T_s} = 3 \times e^{-T_*/T_s} \quad (1)$$

where,  $g_1 = 3$ ,  $g_0 = 1$  denotes statistical weight of the respective states,  $\nu_{21} = 1420$  MHz is frequency of the photon, and  $T_* = 2\pi\nu_{21}$ . The global 21-cm signal ( $T_{21}$ ), measured relative to the cosmic background radiation (Pritchard & Loeb (2012); Furlanetto & Pritchard (2006); Mesinger et al. (2011); Mesinger & Furlanetto (2007)) is given by:

$$T_{21} \approx 27x_{\text{HI}} \left( \frac{0.15}{\Omega_m h^2} \frac{1+z}{10} \right)^{1/2} \left( \frac{\Omega_b h^2}{0.023} \right) \left( 1 - \frac{T_r}{T_s} \right) \text{mK} \quad (2)$$

where,  $\Omega_b = 0.04897$  and  $\Omega_m = 0.30966$  represent baryon and total matter density parameter in the unit of critical density,  $x_{\text{HI}}$  denotes the fraction of neutral hydrogen atom,  $h = 0.6766$  represents the Hubble parameter (Aghanim et al. (2020)), and  $T_r$  denotes background radiation. After recombination, the baryon number density predominantly contained neutral hydrogen atoms, residual electrons ( $n_e$ ) and residual protons ( $n_p$ ) making the global 21-cm signal a useful probe to study CD and EoR. It can provide information about first-star formation, X-ray and  $\text{Ly}\alpha$  heating, radio background heating, and other exotic heatings. Throughout this work, we use Eq. (2) to construct the global 21-cm signal.

The most crucial quantities in Eq. (2) are  $x_{\text{HI}}$ ,  $T_s$ , and  $T_r$  which determines the intensity of  $T_{21}$ . The spin temperature ( $T_s$ ) given by

$$T_s^{-1} = \frac{T_r^{-1} + x_\alpha T_\alpha^{-1} + x_c T_g^{-1}}{1 + x_\alpha + x_c} \quad (3)$$

$$x_c = \frac{T_*}{T_r} \frac{n_i k_{10}^H}{A_{10}} \quad \text{and} \quad x_\alpha = \frac{T_*}{T_r} \frac{4P_\alpha}{27A_{10}}$$

where,  $x_\alpha$ ,  $x_c$  denotes the  $\text{Ly}\alpha$  and collision coupling coefficient about the excess-radio background radiation (Hirata (2006); Mesinger et al. (2011)) respectively, whereas  $n_i$ ,  $k_{10}^H$ ,  $P_\alpha$ ,  $A_{10}$  respectively represent number density of the species "i", the spin de-excitation rate coefficient due to collisions of species "i" with the hydrogen atom, scattering rate of  $\text{Ly}\alpha$  (Lyman Alpha) radiation, and the Einstein coefficient for spontaneous emission from triplet to the singlet state.  $T_\alpha$  and  $T_g$  respectively denote the colour temperature of  $\text{Ly}\alpha$  photons and kinetic temperatures of IGM. Typically,  $T_\alpha \approx T_g$ , because the optical depth of  $\text{Ly}\alpha$  photons is large, which leads to a large number of scattering thus bringing the radiation field and kinetic temperature of IGM to local equilibrium. In this work, we use this approximation. The three dominant non-exotic processes that determine ( $T_r/T_s$ ) are: (1) absorption and spontaneous emission of background radiation; (2) collision with the hydrogen atoms, residual electrons and protons; (3) the Wouthuysen-Field (WF) effect (Wouthuysen (1952); Field (1959)) which represents excitation and de-excitation of hyperfine states of HI atom due to  $\text{Ly}\alpha$  photon field.

As discussed in section (1), the excess radio background radiation cannot be denied completely. ARCADE 2 and LWA1 measurements inspired uniform redshift-independent synchrotron-like radiation have been considered to represent such radiation, as shown in Fig. (1), whose phenomenological model is provided here (Fialkov & Barkana (2019); Mondal et al. (2020); Banet et al. (2021); Reis et al. (2020); Yang (2018))

$$T_r = T_{\text{CMB},0}(1+z) \left[ 1 + A_r \left( \frac{\nu_{\text{obs}}}{78 \text{ MHz}} \right)^\beta \right] \quad (4)$$

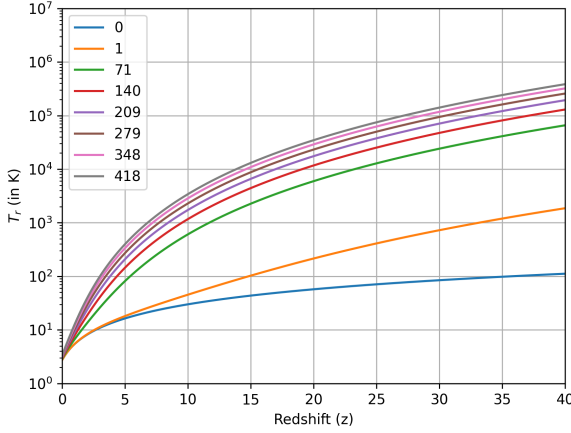


**Figure 1.** The excess background radiation  $T_r$  as a function of redshift ( $z$ ) for different values of the amplitude  $A_r$  given in Eq. (4). Here,  $A_r = 0$  represents the standard CMB radiation  $T_{\text{CMB}}(z)$ . On increasing  $A_r$  from 0 – 140,  $T_r$  changes significantly. However, as soon as it crosses  $A_r = 200$  the curves become closely spaced.

where,  $T_{\text{CMB},0} = 2.723 \text{ K}$  is the present-day CMB temperature and  $\beta = -2.6$  is the spectral index. For 21-cm signal  $\nu_{\text{obs}} = 1420 \text{ MHz}/(1+z)$  and  $A_r$  is the amplitude defined in the reference of CMB at frequency 78 MHz. Considering uniform radiation excess from the dark age, cosmic dawn, and reionization, author (Fialkov & Barkana (2019)) have limited the excess background amplitude to be  $1.9 < A_r < 418$  at the reference frequency of 78 MHz. As discussed here (Dowell & Taylor (2018)), LWA1 sets the limit on  $A_r \sim 418$ . The Low Frequency Array (LOFAR) imposes a strict limit on excess radiation of  $A_r < 182$  (95% CL) and  $A_r < 259$  (99% CL). We can rewrite equation (4) as below, where  $T_{\text{CMB}} = T_{\text{CMB},0}(1+z)$

$$\frac{T_r}{T_{\text{CMB}}} = \left[ 1 + A_r \left( \frac{1+z}{18.2} \right)^{2.6} \right] \quad (5)$$

In the review (Pritchard & Loeb (2012)), the evolution of the global 21-cm signal in CMB bath has been described in detail; here, we will briefly explain the same. At the end of recombination, which occurred at a redshift ( $z \approx 1100$ ) neutral hydrogen atoms were formed, and the photons were free to travel known as CMB ( $T_{\text{CMB}} = T_{\text{CMB},0}(1+z)$ ). This period is often called the last scattering surface. Due to the Compton scattering, the CMB and IGM were in thermal equilibrium,  $T_{\text{CMB}} \approx T_g$ , till  $z \sim 200$  causing an absence of the 21-cm signal. This era is called the Dark Ages. Due to cosmic expansion,  $T_g$  and  $T_{\text{CMB}}$  cooled down  $\propto (1+z)^2$  and  $\propto (1+z)$  respectively, over the time. For redshifts  $40 \lesssim z \lesssim 200$ ,  $x_e \gg 1$ , which causes an absorption signal. Nevertheless, this absorption signal has not been observed yet due to radio antennas' poor sensitivity, which falls dramatically for frequencies below 50 MHz. At  $z < 40$  till the formation of first star the  $x_e \approx 0$  causing no 21-cm signal (Barkana et al. (2018); Pritchard & Loeb (2012)). Ly $\alpha$  radiation coupled the gas via WF effect after the first star formation at redshift  $z \sim 30 - 25$  making  $x_e \gg 1$ . During this time, an absorption signal can be observed, and this phase is called the Cosmic Dawn (CD). Around  $z \sim 15$ , X-ray radiation from AGN could have heated the gas, causing an emission signal. After a certain period, at  $z \sim 7 - 5$ ;  $x_e \rightarrow 1$  resulting in no

signal. This era is called the Epoch of Reionization (EoR). Instead of considering a wide range of redshifts, in this work, we consider EDGES reference  $z \sim 27 - 14$  (Bowman et al. (2018)).

### 3 EVOLUTION OF GAS TEMPERATURE

The standard evolution of gas temperature ( $T_g$ ) and ionization fraction ( $x_i \approx (1 - x_e)$ ) with redshift without any exotic energy injection can be written as

$$\begin{aligned} \frac{dx_e}{dz} &= \frac{\mathcal{P}}{(1+z)H} \left[ n_H x_e^2 \alpha_B - (1 - x_e) \beta_B e^{-E_\alpha/T_{\text{CMB}}} \right] \\ \frac{dT_g}{dz} &= 2 \frac{T_g}{1+z} + \frac{\Gamma_c}{(1+z)H} (T_g - T_{\text{CMB}}) \\ \Gamma_c &= \frac{8N_e \sigma_T a_r T_{\text{CMB}}^4}{3m_e N_{\text{tot}}} \\ \mathcal{P} &= \frac{1 + \mathcal{K}_H \Lambda_H n_H (1 - x_e)}{1 + \mathcal{K}_H (\Lambda_H + \beta_H) n_H (1 - x_e)} \end{aligned} \quad (6)$$

Here,  $\mathcal{P}$  is Peebles coefficient (D'Amico et al. (2018); Peebles (1968)),  $\mathcal{K}_H = \pi^2/(E_\alpha^3 H)$  and  $\Lambda_H = 8.22/\text{sec}$  represents red-shifting of Ly $\alpha$  photons and 2S-1S level two-photon decay rate in hydrogen atom (Tung et al. (1984)).  $\alpha_B$  and  $\beta_B$  are the case-B recombination and photo-ionization rate respectively (Mitridate & Podo (2018); Seager et al. (1999, 2000)).  $N_{\text{tot}} = N_H(1 + f_{\text{He}} + x_e)$ ,  $f_{\text{He}} = 0.08$ ,  $T_{\text{CMB}} = T_{\text{CMB},0}(1+z)$ .  $a_r = 7.57 \times 10^{-16} \text{ Jm}^{-3} \text{ K}^{-4}$  is the radiation density constant,  $\sigma_T$  is the Thomson scattering cross-section, and  $m_e$  is the mass of electron. During the early stages ( $z \gtrsim 200$ ),  $T_g$  was in equilibrium with the cosmic microwave background temperature (CMB) due to Compton scattering. However, the influence of non-thermal excess radio radiation on the gas temperature is insignificant in the second term and thus can be ignored (Feng & Holder (2018)). After the formation of the first stars (at  $z \sim 30$ ), their radiation begins to heat the IGM. In addition to X-ray heating, the gas temperature may increase by  $\sim 10\%$  due to heating by CMB photons only mediated via Ly $\alpha$  photons, even in the absence of X-ray heating or excess radio background—from now on we write this heating effect as "VDKZ18" (Venumadhav et al. (2018)). We analyse our final results in both scenarios: with and without the VDKZ18 heating effect due to excess radio background. In presence of X-ray heating and VDKZ18, the  $T_g$  in equation (6) will be modified as:

$$\begin{aligned} \frac{dT_g}{dz} &= 2 \frac{T_g}{1+z} + \frac{\Gamma_c}{(1+z)H} (T_g - T_{\text{CMB}}) + \left. \frac{dT_g}{dz} \right|_{\text{X-ray}} + \frac{N_H \Gamma_r}{(1+z)N_{\text{tot}}} \\ \Gamma_r &= \left( 1 - \frac{T_r}{T_s} \right) \frac{A_{10} T_*}{2H} x_{\text{HI}} x_r \end{aligned} \quad (7)$$

here,  $x_r = 1/\tau_{21} \times [1 - \exp(-\tau_{21})]$ , and the 21-cm optical depth  $\tau_{21} = 8.1 \times 10^{-2} x_{\text{HI}} [(1+z)/20]^{1.5} (10\text{K}/T_S)$ . Motivated by references (Kovetz et al. (2018); Mirocha et al. (2015); Harker et al. (2016)), to account for the impact of X-ray heating and ionization of the IGM we adopt tanh parameterization. For the evolution of ionization fraction due to X-ray heating, we use  $x_e = x'_e (1 + \tanh[(x'_{z0} - z)/\delta z])$  with  $(x'_e, x'_{z0}, \delta z) = (1, 9, 3)$  as the corresponding values. The chosen model is based on the one proposed in Ref. (Kovetz et al. (2018)), and the same fiducial model is considered for the present case. In Fig. (2), we examined the impact of VDKZ18 and X-ray heating on

IGM. Focusing on the light blue and orange solid line of Fig. (2a), which represents the standard evolution of IGM temperature due to Hubble expansion and Compton scattering and VDKZ18 heating without excess background radiation ( $A_r = 0$ ), i.e. only CMB as background radiation. As we vary the value of  $A_r$  from 1.9 – 418, the IGM temperature increases substantially. However, it can be seen that for  $A_r$  in the range (100–418) the curves clumped suggesting no significant change in  $T_g$ . This is because  $\Gamma_r \propto (T_r/T_s - 1) \sim T_r/T_s$  in Eq. (7), and as we increase  $A_r$ ,  $T_r/T_s$  increases slowly— as also shown by (Natwariya (2021)). We have also investigated the role of X-ray heating after the inclusion of the VDKZ18— shown by Fig. (2b). We found an increase in  $T_g$  due to the inclusion of the VDKZ18 effect even in the presence of X-ray heating as shown by the light blue and orange solid lines. The IGM temperature changes significantly when we increase  $A_r$  from 1.9 – 20 depicted by the red ( $A_r = 1.9$ ) and green ( $A_r = 20$ ) solid line. However, as soon as we increase the  $A_r$  value further,  $T_g$  almost remains constant as shown by the blue ( $A_r = 100$ ) and cyan ( $A_r = 418$ ) solid line. Thus along with X-ray heating, it is important to incorporate VDKZ18 heating when there is excess background radiation, especially in LOFAR limit, as it can lead to a substantial increase in  $T_g$  in the redshift range  $15 < z < 19$ , which is of particular interest.

#### 4 GENERATING THE GLOBAL 21-CM SIGNAL

Many theoretical models propose that the shape and amplitude of the global 21-cm signal may change. (Fialkov et al. (2014, 2015)) and (Cohen et al. (2017)) employed a semi-numerical technique to predict possible 21-cm global signals between the redshift range of  $z \sim 6 - 40$ . The signal is parameterized using physical characteristics— closely connected to the IGM features, allowing us to deduce the physics of the earliest source. (Bernardi et al. (2015, 2016)) represent the absorption characteristic as Gaussian. Similarly, (Pritchard & Loeb (2010)) proposed a turning point model, which indicates positions in redshift, and amplitude and shape of brightness temperature. The section of the global signal between the turning points is represented as a cubic spline, which allows great flexibility and may describe a variety of 21-cm signals. Nevertheless, additional interpretation is required to link the turning point positions to the physics of the initial luminous sources. Mirocha et al. (2013, 2015); Harker (2015) proposed the tanh parameterization, which uses a succession of tanh functions to simulate the global signal.

Although it is possible to use a fixed value for  $x_e \sim 10^{-4}$  here (Bharadwaj & Ali (2004)), we instead consider solving all coupled equations. We solve the IGM temperature evolution Eq. (7) and evolution of ionization fraction in Eq. (6) to construct a simulated global 21-cm signal in this work. The initial conditions for  $T_g$  and  $x_e$  are taken from RECFast++ (Seager et al. (1999)). Ly $\alpha$  background influences the amplitude of  $T_{21}(z)$  via WF coupling ( $x_\alpha$ ) and  $T_{21}$  as described in Eq. (3), thus we adopt a tanh parameterization inspired from Ref. (Kovetz et al. (2018); Natwariya (2021); Harker et al. (2016)). Other than  $A_r$  in Eq. (4) which act as a free parameter (Feng & Holder (2018); Singal et al. (2018); Fixsen et al. (2011)), the two quantities ( $x_\alpha$  and  $T_{Xray}$ ) are allowed to evolve as a tanh function given by,

$$C = C_{\text{ref}} \left( 1 + \tanh \left\{ \frac{C_{z0} - z}{C_{dz}} \right\} \right) \quad (8)$$

where,  $C$  represents the cosmological parameters  $x_\alpha$  and  $T_{Xray}$ .

$C_{dz}$ ,  $C_{\text{ref}}$  and  $C_{z0}$  represent the duration, step height and pivot redshift, respectively. Because these characteristics are directly related to IGM properties rather than luminous source features, they bridge the physical and phenomenological models such as spline or Gaussian models. In this work, we used one non-tanh function ( $A_r$ ) and two tanh functions ( $T_{Xray}$  and  $x_\alpha$ ). The tanh parameterized parameters, as a function of three independent parameters, are mentioned below.

$$\begin{aligned} x_\alpha &= 2 \frac{x_{\text{ref}}}{1+z} \left( 1 + \tanh \left\{ (x_{z0} - z) / x_{dz} \right\} \right) \\ T_{Xray} &= T_{\text{ref}} \left( 1 + \tanh \left\{ (T_{z0} - z) / T_{dz} \right\} \right) \end{aligned} \quad (9)$$

Here we focus on CD and EoR, therefore, the standard global 21-cm signal is generated using the hyperbolic tangent (tanh) function in the redshift range  $z \sim 26 - 12$ , as presented in Fig. (3a). As explained in section (2), the 21-cm signal  $T_{21} \neq 0$  for  $14 \lesssim z \lesssim 30$ . At these redshift ranges, both X-ray and VDKZ18 heating dominate significantly. Therefore, we consider both IGM heating mechanisms in Eq. (7) for the evolution of the IGM temperature along with the standard IGM evolution equation. The inclusion of the VDKZ18 can change the amplitude and position of  $T_{21}(z)$  even in the presence of a strong heating effect like X-ray heating (Fig. (3a)). In Fig. (3b), we considered values of  $A_r$  in the range 1.9 – 200 indicating that such excess radiation would increase its amplitude significantly. It can be noted that  $A_r = 1.9$  is enough to explain the EDGES limit ( $-500$  mK).

We have considered  $T_{\text{ref}} = 10^3$  K and  $x'_e = 1$ ,  $x'_{z0} = 9$ ,  $\delta z = 3$  to be fixed as its value saturates at lower redshifts. All other parameters, along with  $A_r$  have been considered as free parameters, i.e.,  $x_{\text{ref}}$ ,  $x_{z0}$ ,  $x_{dz}$ ,  $T_{z0}$ , and  $T_{dz}$ , which we varied to generate global 21-cm signals of different shapes and amplitudes. The inferred value of the aforementioned free parameters for generating the standard curve (Fig. (3a)) is taken to be (100, 17, 2, 12.75, 1) respectively (Kovetz et al. (2018); Natwariya (2021)). We varied ( $x_{\text{ref}}$ ,  $x_{z0}$ ,  $T_{z0}$ ) and ( $x_{dz}$ ,  $T_{dz}$ ) by ( $\pm 30\%$  and  $\pm 5\%$ ) respectively from the aforementioned central value, to generate the training signal keeping the range  $-200$  mK  $< T_{21} < -1000$  mK; in reference to EDGES limit. For  $A_r$ , we considered the minimum and maximum values to be 0 and 200. We have considered the minimum value to be 0 as it depicts CMBR as the background radiation. The parameter range examined in this study adequately depicts a wide variety of global signal shapes, as shown in section (6.2). Rather than solely parameterizing the  $T_{21}(z)$  using a tanh function, we opted to use parameterization for the source (first star) related quantities, i.e., X-ray and Ly $\alpha$  while maintaining the conventional cosmological intergalactic medium evolution. In future work, we aim to include parameters that directly link to the astrophysical nature of first-star.

#### 5 FOREGROUND MODELLING

Detecting the weak global 21-cm signal during CD and EoR is challenging due to the strong foreground radiation and various instrumental and atmospheric distortions. The radio emissions from the Milky Way and other extragalactic sources are significantly brighter than the cosmological signal. The expected strength of the global 21-cm signal is approximately  $10^{-4}$  times weaker than the foreground emissions. Experiments face significant challenges in extracting the global 21-cm signal due to bright foregrounds, Radio Frequency Interference (RFI), and instrumental calibration errors. These challenges require sophisticated simulations to determine the impact of



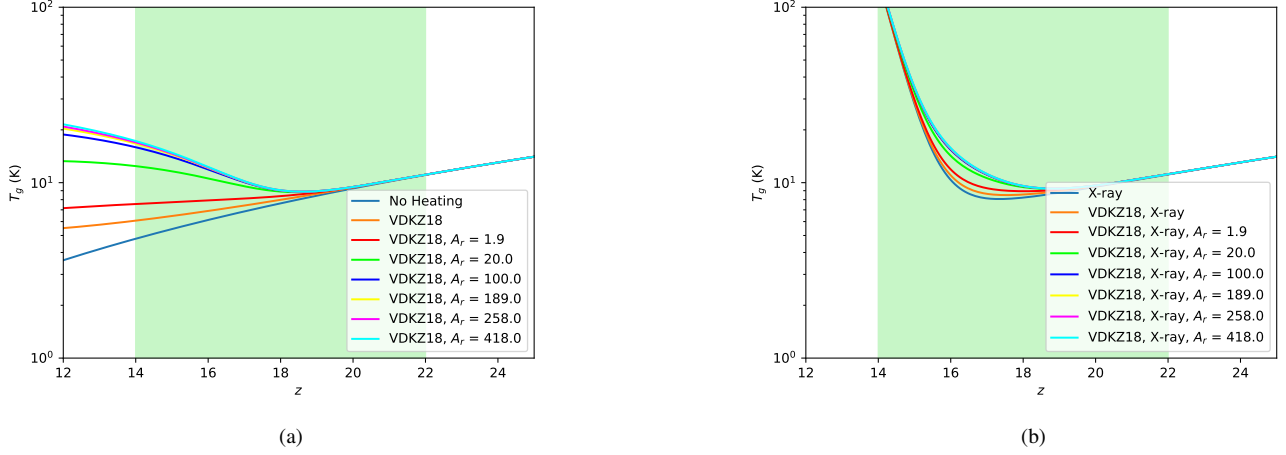


**Figure 2.** Thermal evolution of IGM temperature in the presence of X-ray and VDKZ18. Fig. (2a) shows that  $T_g(z)$  starts to vary due to VDKZ18 from  $z \sim 20$  after the first star formation. The inclusion of excess-background radiation does change  $T_g$  with  $A_r$ . Fig. (2b) shows that X-ray heating changes  $T_g$  significantly, but it can be clearly seen that the existence of excess radiation shifts the  $T_g$  curve. In both plots, the shaded region shows  $15 < z < 20$  region.

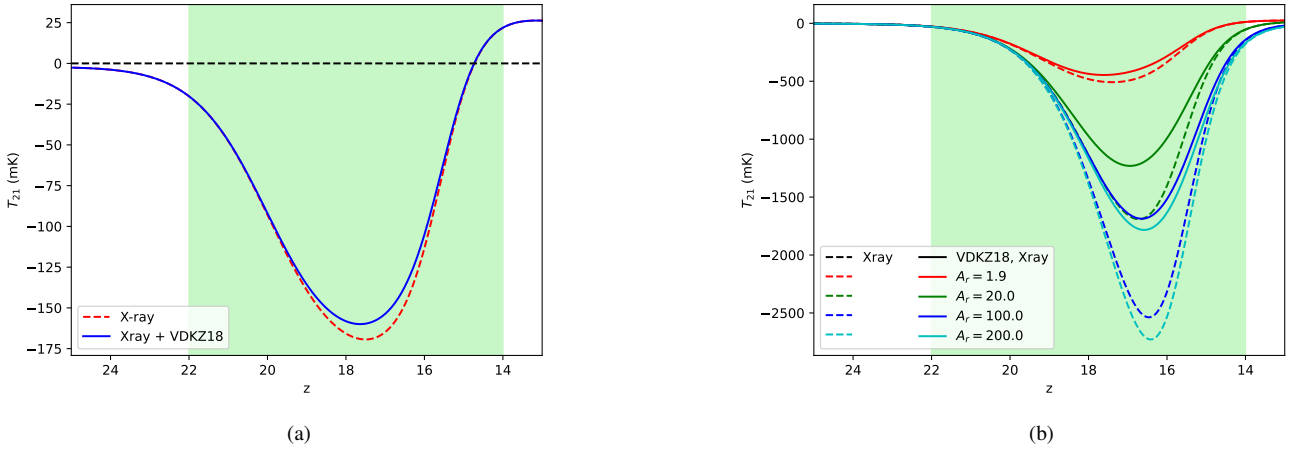


**Figure 3.** The parameterized global 21-cm signal in the presence of excess-radio background radiation. Fig. (3a) shows the construction of the global 21-cm signal using tanh parameterization in the presence and absence of the VDKZ18 effect without excess-radio background radiation. Fig. (3b) shows a shift and increment in the amplitude of Fig. (3a) while considering  $A_r$  value equals to (1.9, 20, 100, 200). The black solid and dashed lines in the legend refer to the presence and absence of the VDKZ18 respectively along with X-ray. The red, blue, green, and cyan colour solid and dashed line represent different  $A_r$  values.

these factors on the extraction of the desired signal. Therefore, having a precise model for foregrounds at radio frequencies is crucial to ensure accurate prediction. According to (Pritchard & Loeb (2010), Bernardi et al. (2016), Bernardi et al. (2015)), the foreground spectrum can be represented as a polynomial in the  $\ln(T) - \ln(\nu)$ . In Ref. (Harker et al. (2016)), it is demonstrated using a 3<sup>rd</sup> or 4<sup>th</sup>-order polynomial is sufficient enough to model the sky spectrum. Still, it has been found that a 7<sup>th</sup>-order polynomial is necessary when incorporating the chromatic primary beam of the antenna. SARAS 3 (Singh et al. (2022)) have used a 6<sup>th</sup>-order  $\ln(T) - \ln(\nu)$  to model Galactic and extragalactic foreground passing through ionosphere added with systematic calibration error in a band of frequency 55 – 85 MHz with a resolution of 61 kHz.

In our work, following the (Bowman et al. (2018)), we used  $\ln(T) - \ln(\nu)$  model of 5<sup>th</sup>-order polynomial to represent the Galac-

tic synchronous radiation of spectral index  $-2.5$  along with Earth's ionosphere distortion

$$\frac{T_{FG}(\nu)}{K} = b_0 \left( \frac{\nu}{\nu_0} \right)^{-2.5+b_1+b_2 \ln(\nu/\nu_0)} e^{-b_3(\nu/\nu_0)^{-2}} + b_4 \left( \frac{\nu}{\nu_0} \right)^{-2} \quad (10)$$

where,  $b_0$  represents an overall foreground scale factor,  $b_1$  considers correction to the foreground with specified spectral index,  $b_2$  considers the higher-order spectral terms,  $b_3$  for ionospheric absorption effect, and  $b_4$  for emission from the hot electron in the ionosphere. Here, we have used the linearized form of Eq. (10),

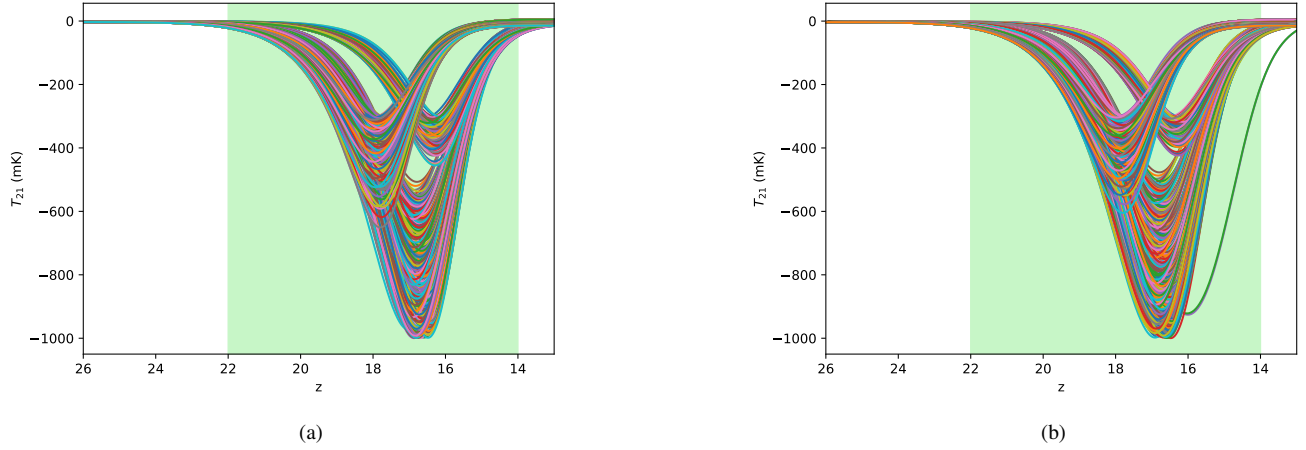


**Figure 4.** Construction of the global 21-cm signal (a) in the absence of the VDKZ18 and (b) in the presence of the VDKZ18. In both cases, we have kept the absorption amplitude to be in the range of  $-200\text{mK} < T_{21} < -1000\text{mK}$  following the EDGES limit.

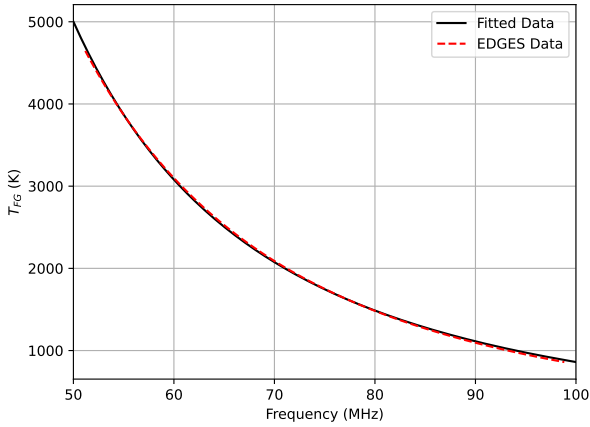


**Figure 5.** Total sky-averaged spectrum considered to represent the foreground radiation.

$$T_{\text{FG}}(\nu) \approx \left(\frac{\nu}{\nu_0}\right)^{-2.5} [b_0 + b_1 \ln(\nu/\nu_0) + b_2 (\ln(\nu/\nu_0))^2 + b_3 (\nu/\nu_0)^{-2} + b_4 (\nu/\nu_0)^{0.5}] \text{K} \quad (11)$$

Using the publicly available data by EDGES<sup>1</sup>, we estimated<sup>2</sup> Eq. (11) coefficients to be  $[b_0, b_1, b_2, b_3, b_4] = [711.8636, 17.5110, -183.0153, 171.6506, 699.3283]$  for  $\nu_0 = 78$  MHz in the band of 51 – 100 MHz, shown in Fig. (5). To generate the training set, shown in Fig. (6), we varied the free parameters by  $\pm 20\%$ . This training data includes an even distribution of  $T_{\text{FG}}$  around the fitted data (Fig. (5)). The foreground is smoother than the

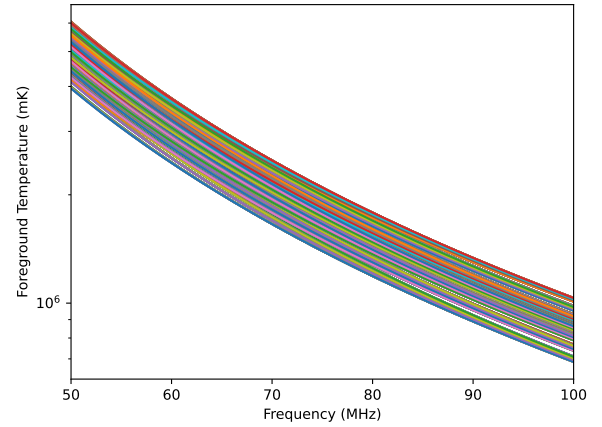


**Figure 6.** The foreground modelling training data set used in the neural network. We have generated this dataset using Eq. (11). As expected, it can be seen that the foreground is  $\sim 10^4$  brighter than the 21-cm cosmological signal.

cosmological signal, and we use this feature to extract the  $T_{21}$  signal, as described in section (7).

## 6 ARTIFICIAL NEURAL NETWORK

### 6.1 Overview

This section briefly introduces the fundamental concepts of artificial neural networks (ANNs). A basic neural network comprises three principal layers: an input layer, one or more hidden layers, and an output layer. In a feed-forward and fully connected neural network, every neuron in a given layer is connected to every neuron in the subsequent layer, and the transmission of information is unidirectional. The neuron serves as the fundamental unit of an ANN. Each of these connections is associated with a weight and a bias. A cost or error function is computed following each forward pass in the output layer. During training, this cost function is optimized itera-

<sup>1</sup> <https://loco.lab.asu.edu/edges/edges-data-release/>

<sup>2</sup> We estimated the coefficients using a simple gradient descent method of Mean Square Error (MSE) cost function. The Python code can be found in <https://github.com/DarkMatter003/Neural-Network-and-21-cm-Cosmology>

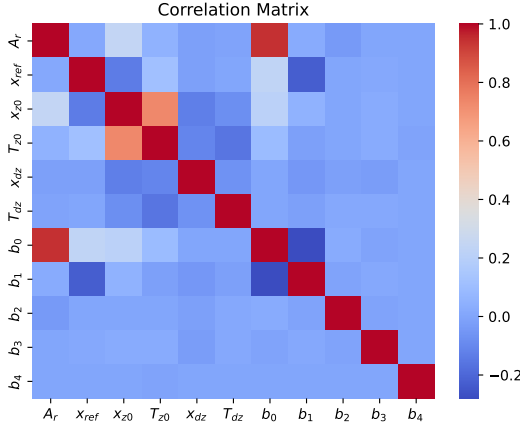


**Figure 7.** The correlation between the foreground and  $T_{21}$  parameters. It can be seen that,  $b_0$  representing the overall foreground scale factor is highly correlated to  $A_r$ , while is significantly responsible for the  $T_{21}$  amplitude.

tively by back-propagating the errors. A thorough explanation of the fundamental algorithm employed in artificial neural networks can be found in (Olvera et al. (2022)). Our feed-forward network utilizes an ANN with two dense layers, implemented using the Sequential Model from the PyTorch in Python. In the input layer, we have incorporated 1024 neurons to correspond with the 1024 frequency channels ranging from 53–98 MHz. We have utilized standard `scikit-learn` (Pospelov et al. (2018)) and PyTorch modules to construct our network, determining the number and size of hidden layers to maximize network performance. The number of neurons in the output layer aligns with the number of output parameters we aim to predict. The following sections comprehensively describe the neural network's structure used in our study.

## 6.2 Construction of Training data set

We have generated the training data set as described in section (4-5) by varying the IGM and foreground parameters in the aforementioned range. The effect of VDKZ18 in the presence of excess background radiation can be seen in Fig. (3); hence two different training sets were built  $T_{21wc}$  and  $T_{21woc}$  which represents 21-cm signal with and without VDKZ18 respectively. In both cases, we have kept the absorption amplitude's lower and upper limits to be  $-200$  mK and  $-1000$  mK. We kept our  $T_{21}$  training set lower limit as  $-200$  mK such it will include the possibility of extracting signal if found in future experiments. Taking into account a frequency range of 53–98 MHz, we built both foreground and 21-cm signal training sets across 1024 channels and of the same order (mK) to avoid a biased prediction. The mock training data set consists of four signals:

$$\begin{aligned} T_{\text{tot}}^1 &= T_{21wc}(\nu) \\ T_{\text{tot}}^2 &= T_{21woc}(\nu) \\ T_{\text{tot}}^3 &= T_{21wc}(\nu) + T_{\text{FG}}(\nu) \end{aligned} \quad (12)$$

The Spearman correlation<sup>3</sup> between all cosmological ( $T_{21}$ ) and fore-

ground parameters can be analyzed from Fig. (7) for the dataset generated (as explained in section (5) and (4)). It can be seen that  $b_0$  is highly correlated to  $A_r$ , as  $b_0$  represents an overall foreground scale factor. This could be one of the reasons why it is difficult to extract the global 21-cm signal from the foreground.  $b_0$  and  $b_1$  being highly correlated can make foreground parameter estimation difficult, which has been shown in section (7.2).

In Fig. (8), which has been used during the training process, it can be seen that  $x_{z0}$  and  $T_{z0}$  are negatively correlated to each other. At the same time, they are negatively and positively correlated to  $A_r$ , respectively, in the case of the absence of the VDKZ18 (Fig. (8a)). In the presence of the VDKZ18 (Fig. (8b)),  $x_{z0}$  and  $T_{z0}$  are positively correlated to each other while being uncorrelated to  $A_r$ . In section (6.3), we added noise to the above training set for parameter prediction. One should note, that the correlation found between the parameters of foreground and  $T_{21}$  signal is due to generated training data thus changing the data size can change the correlation as well.

## 6.3 Predicting Dataset

In this work, we have constructed two sets of predicting data sets, as mentioned above, by adding noise. We added the noise ( $\sigma_t(\nu)$ ) (Bowman et al. (2018)) to every  $T_{\text{tot}}^i$  in Eq. (12) i.e.,

$$T_{\text{pred}}^i = T_{\text{tot}}^i + \sigma_t(\nu) \quad (13)$$

where,  $\sigma_t(\nu)$  is the thermal noise which can be re-written from the standard radiometer equation as a function of bandwidth  $\Delta\nu$  and observational time  $\tau = 10^6 \times 3600 \times N_t$ ;  $N_t$  being the hours of observation.

$$\sigma_t(\nu) = \frac{T_{\text{sys}}(\nu)}{\sqrt{\delta\nu \cdot \tau}} \quad (14)$$

The  $T_{\text{sys}}(\nu)$  can be replaced with  $T_{\text{FG}}(\nu)$  for our work. It can be seen that  $\sigma_t(\nu) \propto 1/\sqrt{N_t}$ , thus for this work we considered  $N_t = 1000$  hr of observational time. While the training set in Eq. (12) monitors the neural network's performance, the prediction data set in Eq. (13) has been used for evaluating the accuracy of parameter estimation. The Root mean square error (RMSE) and  $R^2$  score have been given to each parameter estimation as metrics for all prediction datasets to depict the accuracy. The RMSE and  $R^2$  score can be expressed as

$$R^2 = 1 - \frac{\sum (X_{\text{pred}} - X_{\text{orig}})^2}{\sum (X_{\text{orig}} - \bar{X}_{\text{orig}})^2} \quad (15)$$

$$\text{RMSE} = \sqrt{\frac{1}{N_{\text{pred}}} \sum_{j=1}^{N_{\text{pred}}} \left( \frac{X_{\text{orig},j} - X_{\text{pred},j}}{X_{\text{orig},j}} \right)^2} \quad (16)$$

where  $\bar{X}_{\text{orig}}$  is the average of original parameters which has been summed over all training data. The  $R^2$  value lies in the interval (0, 1] where  $R^2 = 1$  represents perfect inference.

<sup>3</sup> The Spearman correlation coefficient is calculated using DataFrame from Pandas (<https://pandas.pydata.org/docs/reference/>)

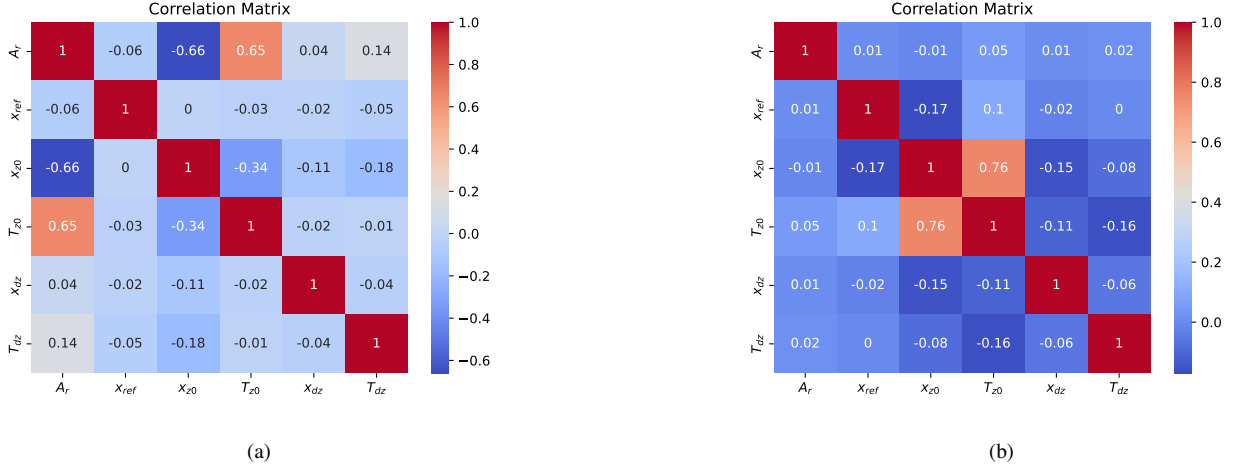


**Figure 8.** The correlation between the parameters of the 21-cm global signal (a) in the absence and (b) in the presence of the VDKZ18 used for generating the training dataset. It can be seen that the correlation between the parameters is different in both cases. While in the case of Fig. (8a) the three parameters are correlated, but in Fig. (8b), only two are correlated.

## 7 RESULT

### 7.1 Only 21-cm Signal

We build two neural networks of (1024, 6) neuron input and output layer corresponding to the frequency channel used in generating the global 21-cm signal shown in Fig. (4). We added three hidden layers of 64, 32, and 16 neurons with activation function ReLU (Shang et al. (2016)) to make the network deep. We used nn module of PyTorch (Paszke et al. (2019)), which contains Sequential API for the feed-forward process. We considered 2000 sample data as input which was split into training and testing dataset (8 : 2) using sklearn (Pedregosa et al. (2011)). Before feeding the training data to the neural network, we preprocessed it using 'MinMaxScaler' from sklearn. To adjust the weight of the hidden layers optimally over the training process, we used Mean Square Error (MSE) as the error function and 'Adam' (Kingma & Ba (2014)) as the optimizer. After tuning all the hyperparameters, the model was trained and saved for prediction. As shown in Fig. (9), the model loss or training loss in presence and absence of VDKZ18 effect approached a constant value after 500 epochs (Fig. (9a)) and 200 (Fig. (9b)) respectively. The model loss depicts the efficiency of the neural network in understanding the input data over epochs. Thus, a lower model loss value represents an efficient neural network. To check the performance of the neural network after training, we predicted 6 parameters ( $A_r, x_{ref}, x_{z0}, T_{z0}, x_{dz}, T_{dz}$ ) by assigning Root Mean Square Error (RMSE) and R-Squared ( $R^2$ ) score to it, as shown in the Fig. (10, 11). The use of a single ANN limits us from extracting a few parameters efficiently, thus  $x_e$  parameters are not considered. We find that the RMSE and  $R^2$  scores around (0.054 – 0.011) and (0.99 – 0.92), respectively, in the presence of VDKZ18; while in the absence of VDKZ18, the values are around (0.012 – 0.068) and (0.99 – 0.87) respectively.

### 7.2 21-cm Signal, Foreground, and Noise

Extraction of the faint cosmological signals buried inside a sea full of bright foreground signals is one of the challenging tasks. It can be seen in Fig. (6) that the foreground is  $\approx 10^3 - 10^4$  times brighter than the  $T_{21}$  signal. In this section, we added foreground (Fig. (6)) to the global 21-cm signal (Fig. (4)) for the neural network training.

Foreground Parameters	$T_{21wc}(\nu) + T_{FG}(\nu) + \sigma_t(\nu)$	
	RMSE	$R^2$ Score
$b_0$	3.0684	0.9984
$b_1$	1.1334	0.8034
$b_2$	4.4728	0.9677
$b_3$	1.2853	0.9972
$b_4$	3.9571	0.9983

**Table 1.** Foreground parameter estimation in the presence of VDKZ18. The reason for  $b_1$  being poorly predicted is its strong correlation with  $b_0$

As our cosmological parameters were already in the same scale, we preprocessed the training data and the foreground parameters with 'StandardScaler' from sklearn prior to training. We scaled the foreground parameters so that during the training process, the weight distribution in the neurons becomes efficient. Using PyTorch, we build another denser neural network than before by adding more layers and neurons. We used 'Adam' (Kingma & Ba (2014)) and 'MSE' as the optimizer and error function. Keeping the hidden layer density to be (512, 512, 256, 128, 64, 32), the activation function as tanh, and the learning rate to 0.0001, we tuned the network's hyperparameter to train and prediction. We added noise to the prediction dataset for parameter estimation to check whether the network has been trained for generalized data instead of memorizing the input data. Our training dataset consisted of 2000 samples and a 1000-sampled predicted data set with added noise, completely unknown to the trained network.

$$T_{pred}^3 = T_{tot}^3 + \sigma_t(\nu) \quad (17)$$

As one NN is being used for parameter estimation, instead of extracting all 11 parameters (6 cosmological and 5 foregrounds) we chose to extract only foreground parameters from  $T_{pred}^3$  such that, once the foreground signal is extracted the residual signal can be fed to the NN constructed in section (7.3) for estimation of the cosmological signal parameters. It can be seen from Fig. (7), that the foreground ( $b_0$ ) and cosmological ( $A_r$ ) parameters are highly correlated. This is due to the fact that  $A_r$  and  $b_0$  are predominantly responsible for



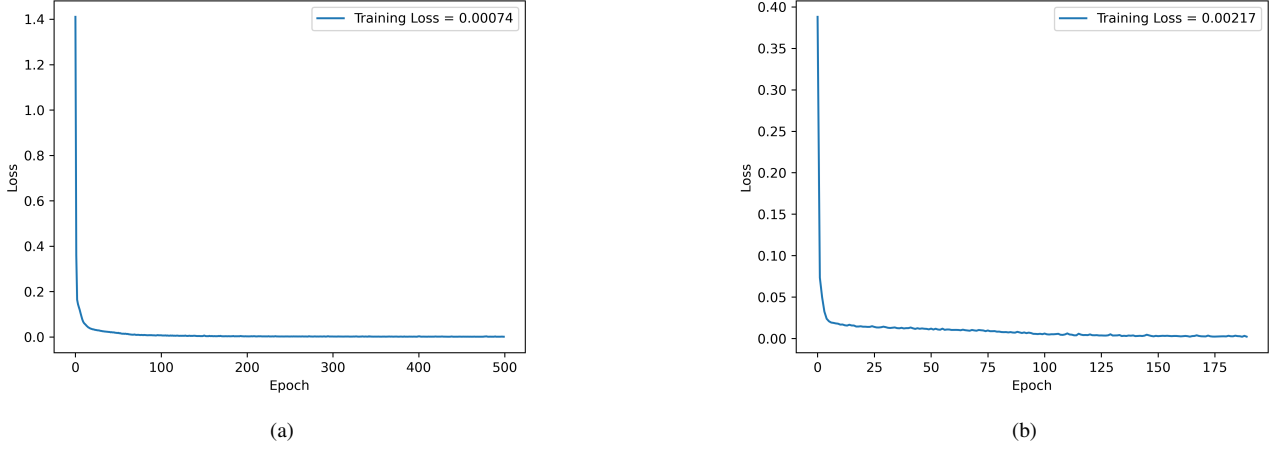


**Figure 9.** Variation of the model loss during the training process, where (a) in the presence of the VDKZ18 and (b) in the absence of the VDKZ18

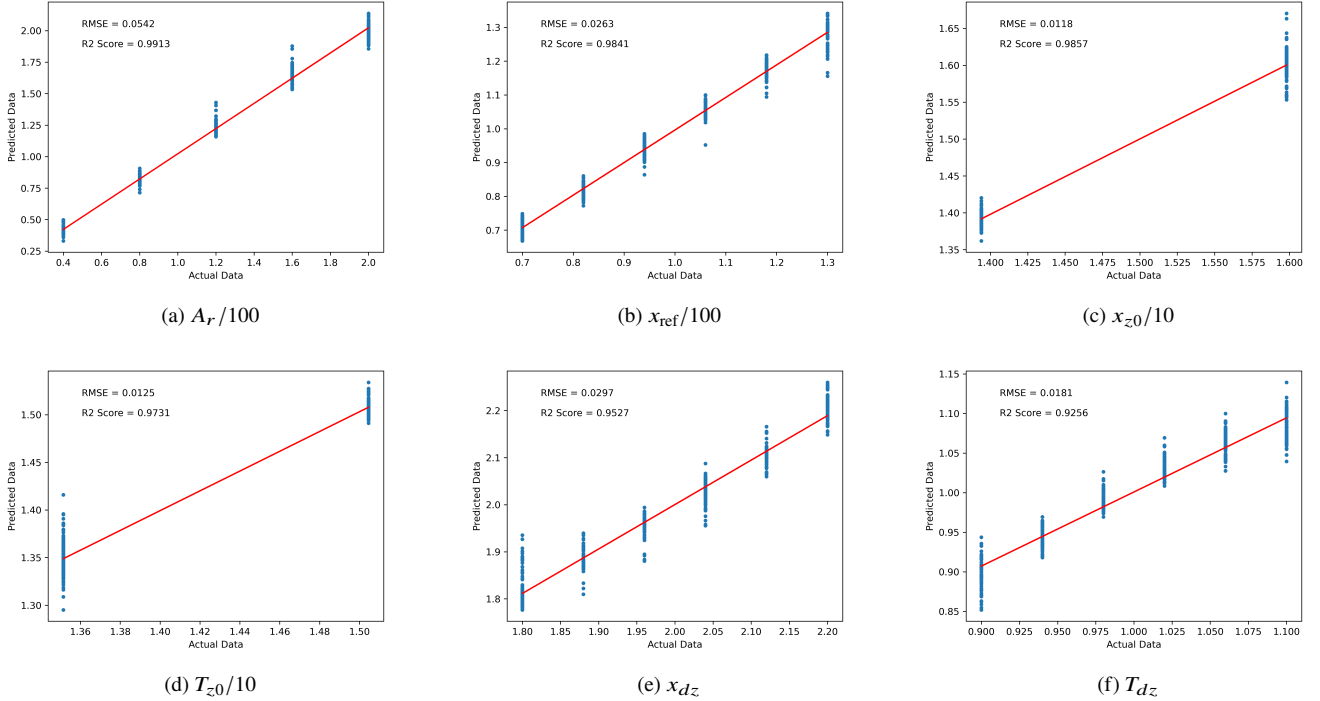


**Figure 10.** Each plot above shows the prediction of the aforementioned parameters with RMSE and  $R^2$  score assigned in the presence of the VDKZ18.

the global 21-cm signal and the foreground signal amplitude. We made the network 6 layered-dense to deal with highly correlated parameters  $b_0$  and  $b_1$ . To check the performance and accuracy after the training, we estimated all the foreground parameters (Fig. 12) and assigned RMSE and  $R^2$  scores to each parameter shown in Table (1). The RMSE scores are higher due to the scale of the foreground parameters, thus the accuracy of prediction can be analysed using  $R^2$  scores. After predicting the parameters of a randomly selected foreground signal, we reconstructed it and compared it with the original signal as shown in Fig. (13). One should note that the predicted parameters might differ from the original as the NN is trained to recognise and learn the relationship between variation of  $T_{FG}$  and

the corresponding parameters, thus during prediction, it will provide possible values of parameters to match  $T_{FG}$ .

### 7.3 21-cm Signal and Noise

In section (7.1), we predicted the parameters after training the neural network with  $T_{21}$  signal. In this section, to check the robustness of the network, we included noise  $\sigma_I(\nu)$ , as defined in section (6.3), to the prediction dataset.

$$T_{\text{pred}}^1 = T_{\text{tot}}^1 + \sigma_I(\nu) \quad (18)$$

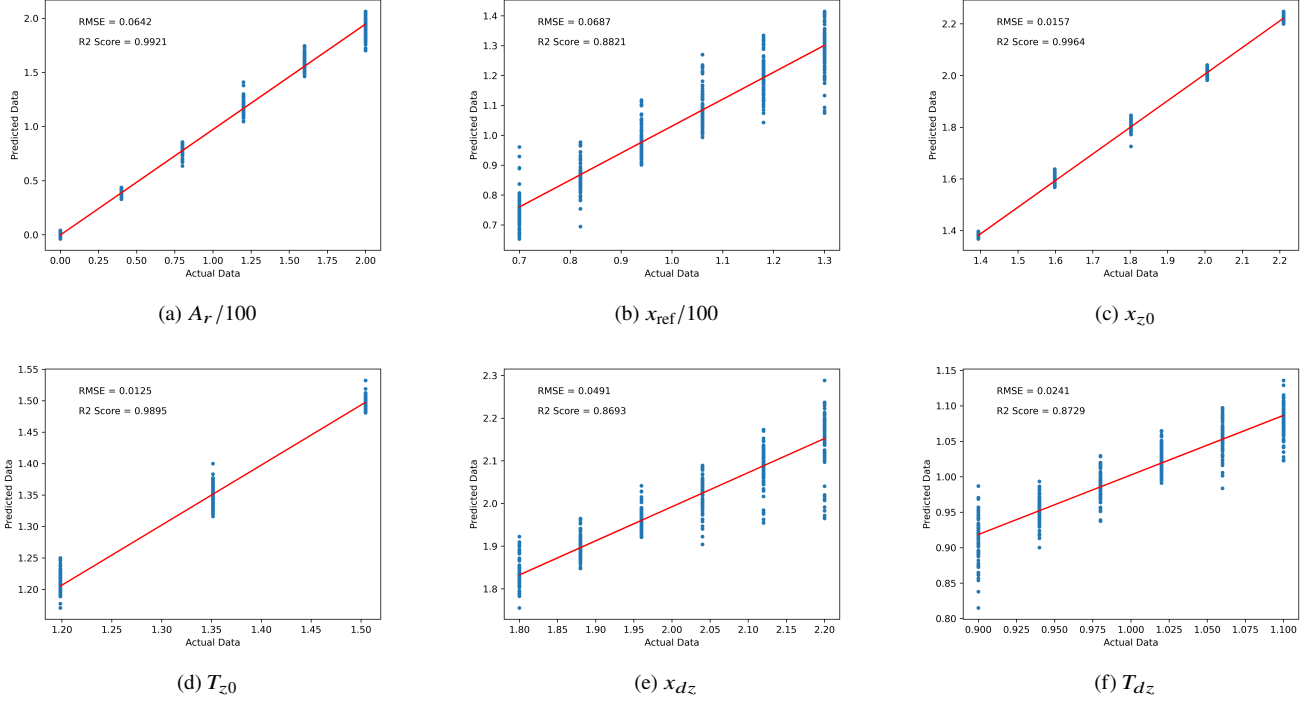


**Figure 11.** Each plot above shows the prediction of the aforementioned parameters with RMSE and  $R^2$  score assigned in the absence of the VDKZ18.

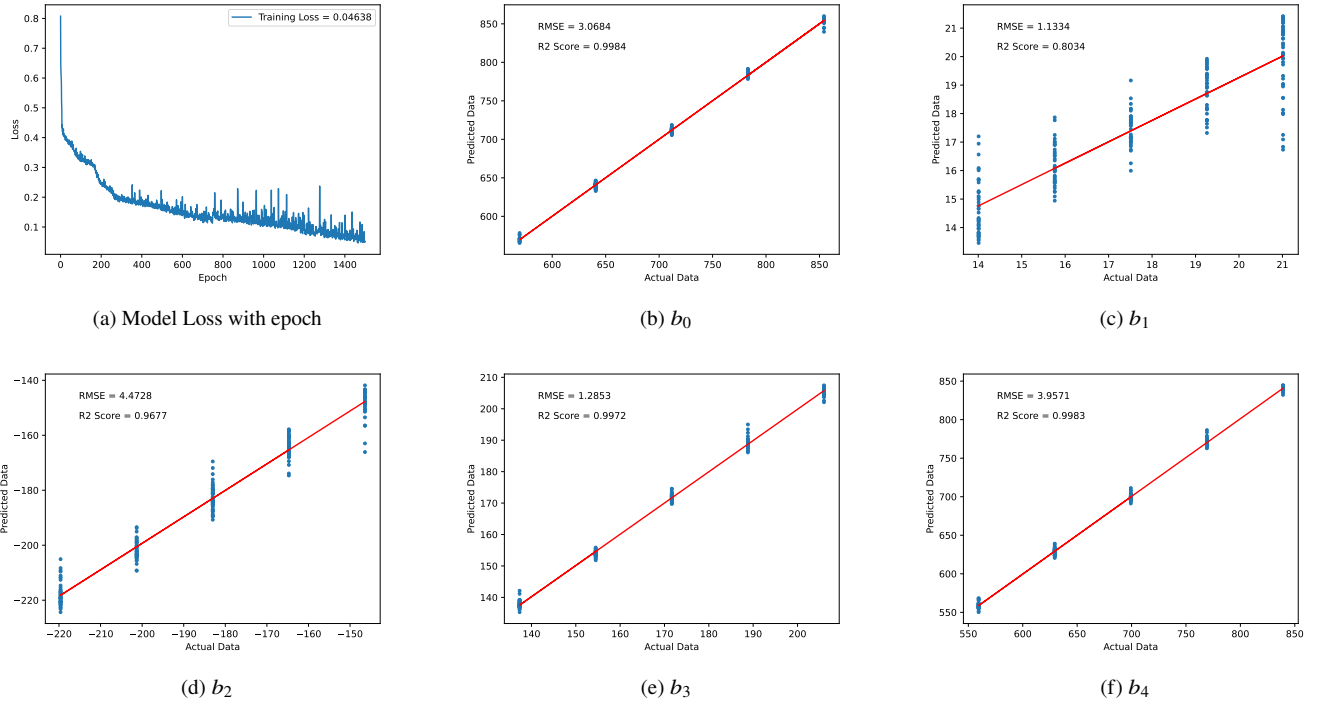


**Figure 12.** Model loss and the prediction of the aforementioned parameters with RMSE and  $R^2$  score assigned in the presence of the foreground and VDKZ18 after the inclusion of noise in the prediction data.

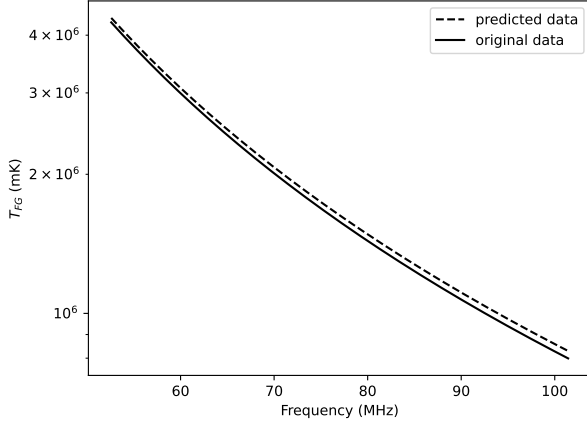


**Figure 13.** In this figure we have shown the comparison between the reconstructed foreground signal from the parameters predicted from the NN and the corresponding original signal. The predicted and original parameters ( $b_0, b_1, b_2, b_3, b_4$ ) are respectively (707.00, 17.18, -176.62, 172.64, 699.44) and (640.67, 19.26, -201.31, 188.81, 699.32).

We constructed another neural network using the technique mentioned in section (7.1). To optimize the training and performance, we kept the number of hidden layers as two, with 64 and 32 neurons to train the NN in the case when VDKZ18 is present. But, in the absence of the VDKZ18 effect case, we chose the number of hidden layers to be three with 128, 64, and 32 neurons. Two different NNs have been considered as the correlation between the parameter changes in the presence and absence of the VDKZ18. The activation function was changed from ReLU to Sigmoid in both cases. We took 2000 training samples and 1000 prediction samples to train and evaluate the network's performance. The variation of the model loss value for both cases during the training has been shown in Fig. (14); it can be seen that the loss approaches a constant value of approx 0.0006 after 300 epochs in both cases. It was found that the RMSE and  $R^2$  score varied in the range (a) in the presence of VDKZ18 (Fig. (15)) to be (0.0036 – 0.0735) and (0.9978 – 0.6960) respectively, and (b) in the absence of VDKZ18 (Fig. (16)) to be (0.0353 – 0.0051) and (0.9326 – 0.9996) respectively. After predicting the parameters ( $A_r, x_{\text{ref}}, x_{z0}, T_{z0}, x_{dz}, T_{dz}$ ) of randomly selected 21-cm signal, we reconstructed the 21-cm signal for both cases from the predicted parameters and compared it with the original signals as shown in Fig. (17). In Fig. (17a) two 21-cm signal has been considered, the red solid and blue dotted curve represents a reconstruction of the 21-cm signal from the predicted parameters (46.41, 79.01, 13.873, 13.526, 2.3446, 0.9099) by the NN trained in the presence of the VDKZ18, while the latter is constructed in the absence of the VDKZ18. Whereas, the red dashed curve represents the original 21-cm signal with parameters (40, 82, 1.3940, 1.3515, 2.2, 0.9). It can be seen that there is a very small variation ( $\sim 14$  mK) in the 21-cm signal amplitude in both cases (i.e., in the presence and absence of VDKZ18). This is due to  $x_{\text{ref}}$  value which is  $\sim 20$  lower than the standard value under consideration (i.e., 100) and as this parameter represents  $\text{Ly}\alpha$  photon intensity (Kovetz et al. (2018)) thus reducing it reduces the VDKZ18 heating which depends on both radio and  $\text{Ly}\alpha$  photon intensity (Venumadhav et al. (2018)) during cosmic dawn. We then considered a different 21-

cm signal (green solid) reconstructed from the predicted parameters (37.29, 127.23, 16.004, 15.042, 2.1872, 0.968) of the original signal (green dashed) with parameters (40, 130, 15.98, 15.045, 2.2, 0.98). As expected the predicted and the original signals almost overlapped. However, when we reconstructed the signal from the predicted parameters in the absence of VDKZ18 (magenta dotted), a variation of ( $\sim 33$  mK) in the amplitude from the predicted signal can be seen. As soon as we increased the  $\text{Ly}\alpha$  photon intensity ( $\sim 30$ ) from the standard value, the VDKZ18 heating became more prominent thereby reducing the 21-cm amplitude.

In Fig. (17b) we considered two signals from the prediction dataset for the parameters prediction by the NN trained in the absence of VDKZ18. First, (red dashed) was considered randomly from the prediction dataset with parameters (40, 82, 15.98, 15.045, 2.04, 1.1) and fed into NN for prediction. The signal (red solid) was reconstructed with the predicted parameters (41.43, 74.54, 15.924, 15.02, 2.0931, 1.0751). Then, we reconstructed the 21-cm signal in the presence of VDKZ18 from the predicted parameters for comparison. The amplitude varied only by  $\sim 10$  mK. However, when a difference signal was considered from the predicted dataset with a greater  $x_{\text{ref}}$  value, we found a greater variation in the amplitude ( $\sim 33$  mK). This can be observed from the green solid curve (predicted signal) with parameters (41.55, 124.52, 14.012, 13.417, 2.2460, 0.9435), the green dashed curve (original signal) with parameters (40, 130, 13.940, 13.515, 2.2, 0.9), and magenta dotted curve (reconstructed in presence of VDKZ18).

One should note that the predicted parameters might differ from the original as the NN is trained to recognise and learn the relationship between the variation of  $T_{21}$  and the corresponding free parameters. Thus during prediction, it can predict combinations of all possible parameter values to match the required 21-cm signal. Therefore a deviation from the original parameter values can be seen. The  $\text{Ly}\alpha$  coupling and X-ray heating have been tanh parameterized (refer equation (9)), therefore it depends upon three values i.e., duration, step height, and the pivot redshift. Thus, it can be compared with a physically motivated model which depends upon  $\text{Ly}\alpha$  intensity ( $J_\alpha$ ) and X-ray spectral energy distribution (refer Pritchard & Loeb (2012)). However, the VDKZ18 effect predominantly depends upon  $\text{Ly}\alpha$  and radio photon intensity (Venumadhav et al. (2018)) during cosmic dawn, therefore its inclusion become as it can change the parameters prediction thereby underestimating or overestimating the 21-cm signal (Fig. (17)).

## 8 SUMMARY AND DISCUSSION

In our research, we generate synthetic data by resolving the typical cosmological equations, as presented in sections (4-6). The data was utilized for training the neural networks. We added noise into the training data to verify the networks' reliability to prediction datasets. The accuracy of one of our estimations is evaluated by examining the RMSE and  $R^2$  scores for each case as listed in Table (1). As far as our understanding goes, most authors have employed Markov Chain Monte Carlo (MCMC), nested sampling, or similar methods for parameter space sampling. As ANN (Artificial Neural Network) and MCMC have different methodologies, we cannot directly compare their speed. However, ANN offers the advantage of bypassing the requirement of computing the likelihood function multiple times to derive inferred parameter values. Thus, when dealing with a higher dimensional parameter space, ANN is computationally more efficient and faster. In the context of neural networks, we can consider training

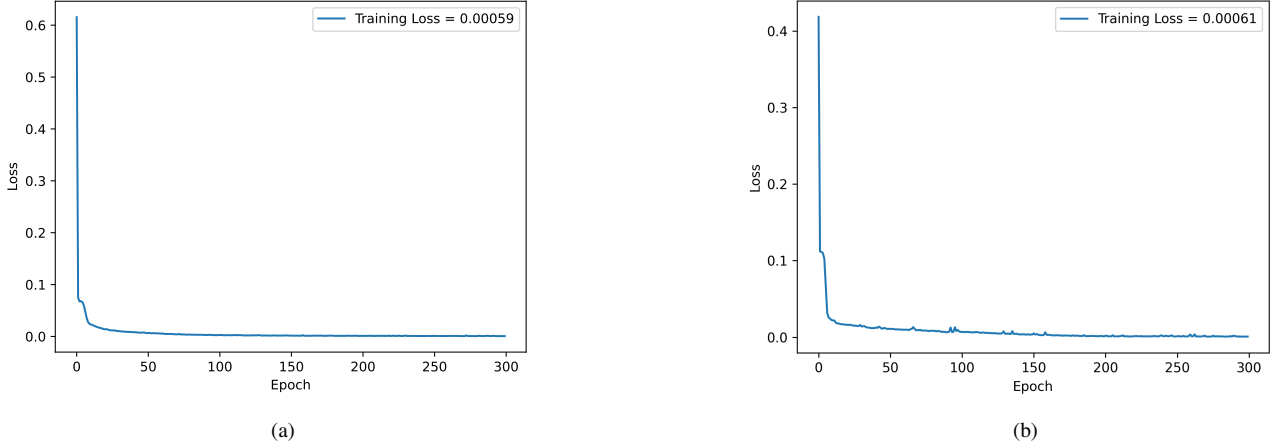


**Figure 14.** Variation in the model loss during the training process, where (a) in the presence of the VDKZ18 and (b) in the absence of the VDKZ18

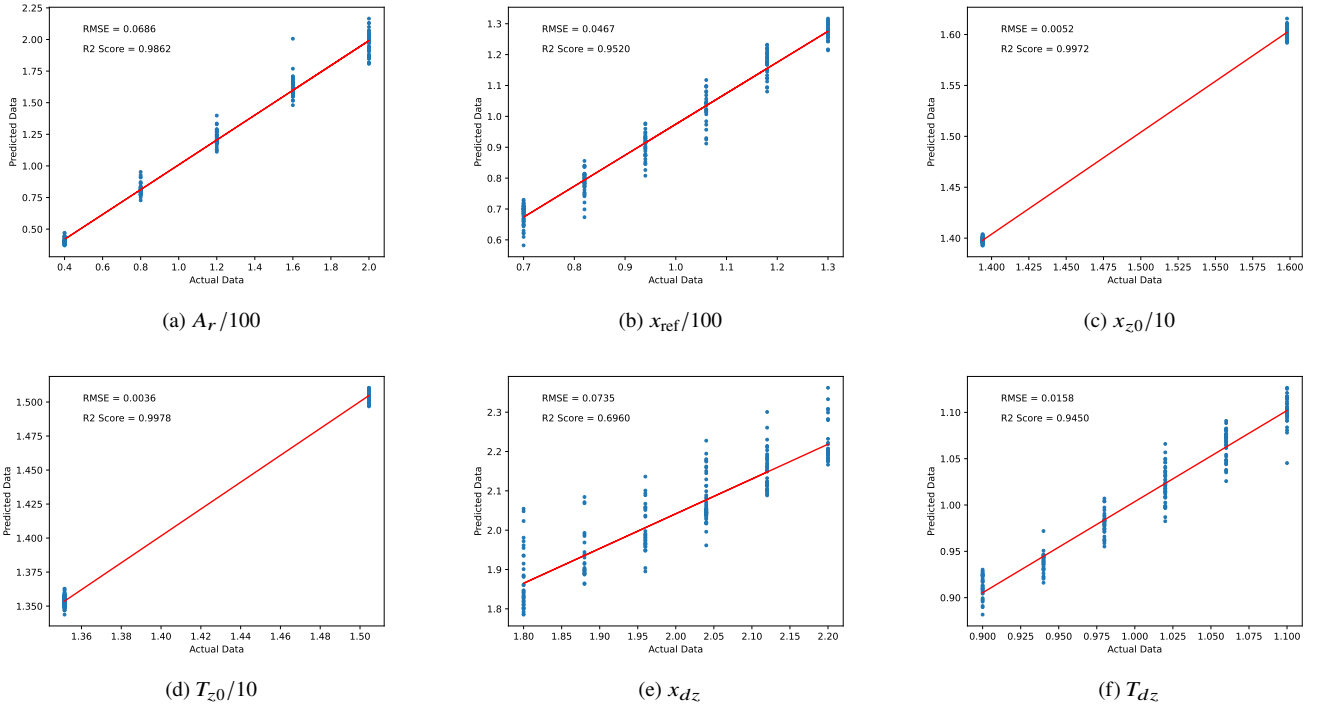


**Figure 15.** Each plot above shows the prediction of the aforementioned parameters with RMSE and  $R^2$  score assigned in the presence of the VDKZ18 after the inclusion of noise in the prediction data .

sets a more realistic substitute for the prior in MCMC. In this work, instead of deploying a single neural network for 21-cm signal parameter estimation, we use two ANNs. Where one ANN was used for removing foreground contamination (section 7.2) and the other was used for estimating the 21-cm signal (section 7.3). While in training, it was observed that if the hyperparameters and the architecture of the NN were unset optimally, then either the estimation accuracy deteriorated or it was too high, depicting underfitting and overfitting conditions. Due to a huge difference in the order of the foreground compared to  $T_{21}$  signal, the efficiency of the network reduces significantly therefore we make the NN deeper by increasing the number of hidden layers.

Our work focused on the importance of the VDKZ18 effect, which depends on radio and  $\text{Ly}\alpha$  photon intensity, on parameter estimations using ANN. However, for simplicity we consider tanh parameterized  $\text{Ly}\alpha$  coupling and X-ray heating term (refer equation 9) along with standard cosmological thermal evolution. The considered parameters for the construction of  $T_{21}$  link closely to the astrophysical properties of the first star during the cosmic dawn following (Mirocha et al. (2015)) a turning point model. We find that the estimation of a 21-cm signal by two neural network training in the presence and absence of VDKZ18 is different due to the difference in estimating the  $x_\alpha$  and  $A_r$  terms. Although we have tanh parameterized  $x_\alpha$ , however, it depends upon  $\text{Ly}\alpha$  photon specific intensity ( $J_\alpha$ ) (Chatterjee et al.



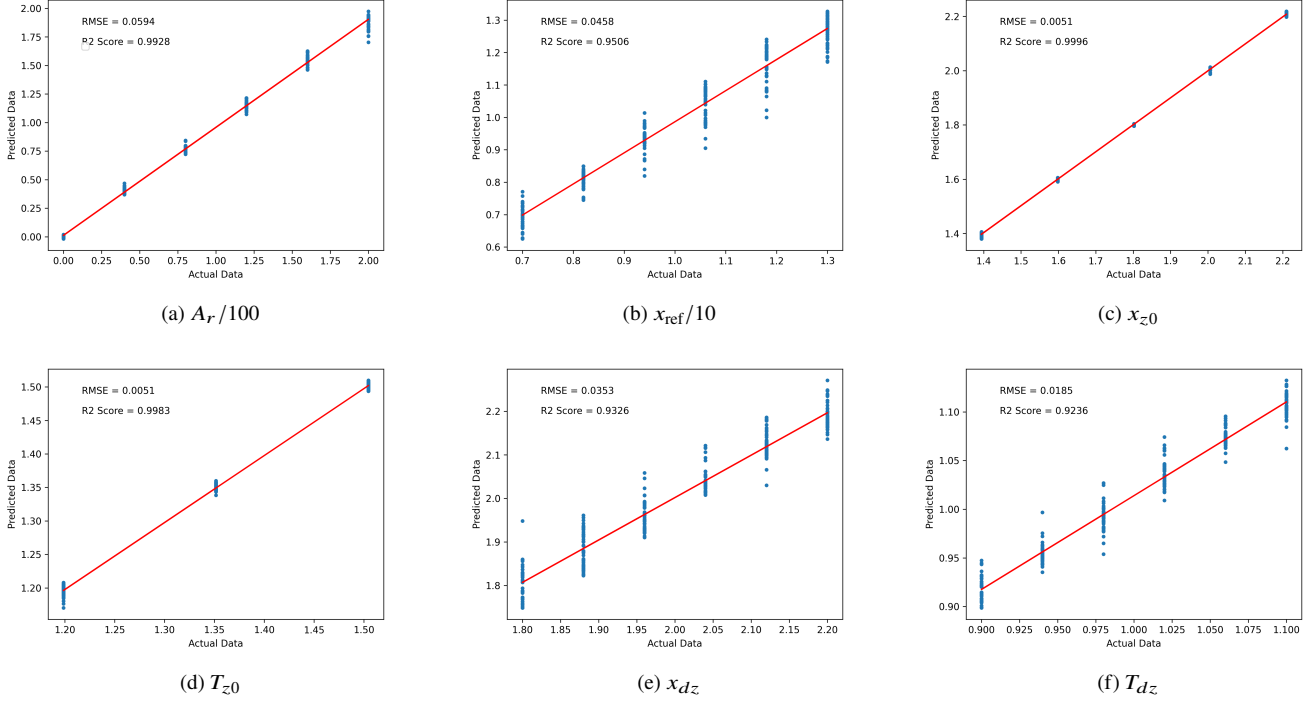


**Figure 16.** Each plot above shows the prediction of the aforementioned parameters with RMSE and  $R^2$  score assigned in the absence of the VDKZ18 after the inclusion of noise in the prediction data .

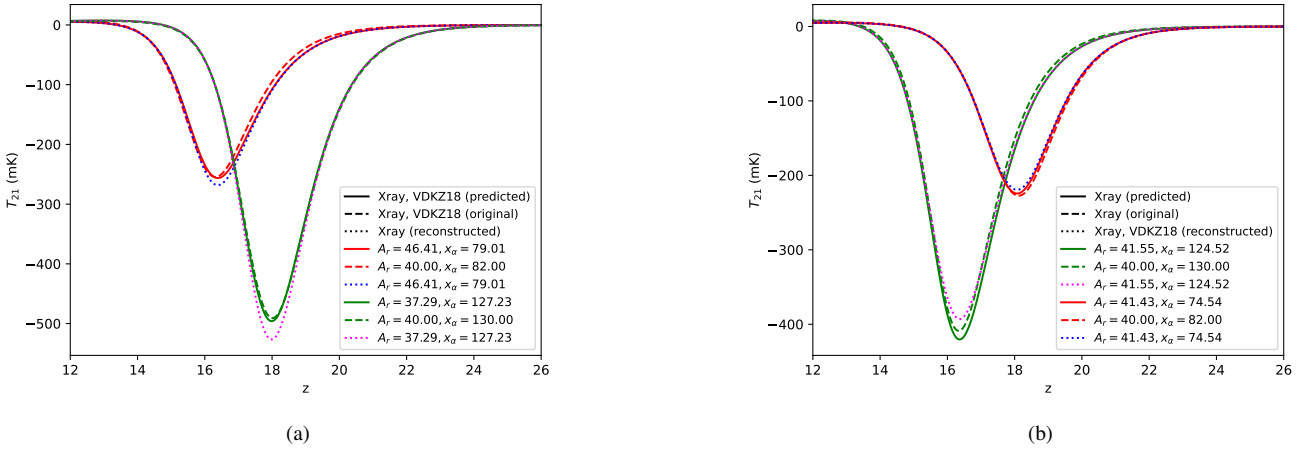


**Figure 17.** Reconstruction of 21-cm signal from the predicted parameters by NN in the presence (Fig. (17a)) and absence (Fig. (17b)) of VDKZ18.

(2019)), and  $A_r$  can be related to excess radio photons using equation (5). In this work (Choudhury et al. (2020)) authors have not considered excess radio radiation scenario, however in this work Choudhury et al. (2021) the authors have constructed training data in the presence of galactic excess radio background. But, they have excluded VDKZ18 heating in the IGM thermal evolution equation, which we have shown to have a significant effect on  $T_{21}$  signal (Fig. (3)), in both of their work. Thus, as shown in Fig. (17), we estimate a variation in parameter estimations Choudhury et al. (2021), especially  $f_R$  and  $N_\alpha$ , in the presence of VDKZ18 heating. Along with this, the emulators (Cohen et al. (2020); Bye et al. (2022)), described in section (1), may need to include this heating effect while training

the NNs for global 21-cm signal generation from the astrophysical parameters. Other than that, we have predicted the foreground parameters thereby reconstructing and removing it from the total sky average signal which has not been done in any previous works, to the best of our knowledge, in the extraction of a global 21-cm signal.

In future work, we intend to apply this concept and algorithm to more realistic data, like EDGES, SARAS 3, REACH. Experiments, like DARE, DAPPER (Burns et al. (2019a)), FARSIDE (Burns et al. (2019b)) being space-based could provide less contaminated data compared to Earth-based experiments. The contamination due to RFI and ionosphere can be neglected for these experiments, making this work ideal for testing. Furthermore, we wish to include energy injection

terms linking directly to the first star's astrophysical properties, instrument response and contamination model to make the NN more robust.

## ACKNOWLEDGEMENT

P. K. N. would like to acknowledge the National Centre for Radio Astrophysics–Tata Institute of Fundamental Research for providing accommodation support during the initial phase of this work. A. C. N. acknowledges financial support from SERB-DST (SRG/2021/002291), India.

## CODE AND DATA AVAILABILITY

We have used the publicly available EDGES data release (<http://loco.lab.asu.edu/edges/edges-data-release/>). The analyses are accomplished in Python, broadly using publicly available modules in NumPy (Harris et al. (2020)), Matplotlib (Hunter (2007)), Astropy (Price-Whelan et al. (2018)), Odeint Solver (Ahnert & Mulansky (2011)) from Scipy (Virtanen et al. (2020)), Natpy (Howson & Scaffidi (2021)), Pandas for data visualization (McKinney et al. (2010)), Heatmap of Seaborn (Waskom (2021)).

## REFERENCES

- Aghanim N., et al., 2020, *Astron. Astrophys.*, 641, A6
- Ahnert K., Mulansky M., 2011, in AIP Conference Proceedings. pp 1586–1589
- Banet A., Barkana R., Fialkov A., Guttman O., 2021, *Mon. Not. Roy. Astron. Soc.*, 503, 1221
- Barkana R., Outmezguine N. J., Redigolo D., Volansky T., 2018, *Phys. Rev. D*, 98, 103005
- Bernardi G., McQuinn M., Greenhill L. J., 2015, *Astrophys. J.*, 799, 90
- Bernardi G., et al., 2016, *Mon. Not. Roy. Astron. Soc.*, 461, 2847
- Bevins H. T. J., Handley W. J., Fialkov A., Acedo E. d. L., Javid K., 2021, *Mon. Not. Roy. Astron. Soc.*, 508, 2923
- Bevins H. T. J., Fialkov A., Acedo E. d. L., Handley W. J., Singh S., Subrahmanyam R., Barkana R., 2022, *Nature Astron.*, 6, 1473
- Bharadwaj S., Ali S. S., 2004, *Mon. Not. Roy. Astron. Soc.*, 352, 142
- Bharadwaj S., Sethi S. K., 2001, *J. Astrophys. Astron.*, 22, 293
- Bhatt J. R., Natwariya P. K., Nayak A. C., Pandey A. K., 2020, *Eur. Phys. J. C*, 80, 334
- Bowman J. D., Rogers A. E. E., Monsalve R. A., Mozdzen T. J., Mahesh N., 2018, *Nature*, 555, 67
- Burns J. O., et al., 2012, *Adv. Space Res.*, 49, 433
- Burns J. O., et al., 2017, *Astrophys. J.*, 844, 33
- Burns J. O., et al., 2019a, Dark Cosmology: Investigating Dark Matter & Exotic Physics in the Dark Ages using the Redshifted 21-cm Global Spectrum ([arXiv:1902.06147](https://arxiv.org/abs/1902.06147))
- Burns J., et al., 2019b, FARSIDE: A Low Radio Frequency Interferometric Array on the Lunar Farside ([arXiv:1907.05407](https://arxiv.org/abs/1907.05407))
- Bye C. H., Portillo S. K. N., Fialkov A., 2022, *Astrophys. J.*, 930, 79
- Chardin J., Uhlrich G., Aubert D., Deparis N., Gillet N., Ocvirk P., Lewis J., 2019, *Mon. Not. Roy. Astron. Soc.*, 490, 1055
- Chatterjee A., Dayal P., Choudhury T. R., Hutter A., 2019, *Monthly Notices of the Royal Astronomical Society*, 487, 3560
- Choudhury M., Datta A., Chakraborty A., 2020, *Mon. Not. Roy. Astron. Soc.*, 491, 4031
- Choudhury M., Chatterjee A., Datta A., Choudhury T. R., 2021, *Mon. Not. Roy. Astron. Soc.*, 502, 2815
- Cohen A., Fialkov A., Barkana R., Lotem M., 2017, *Mon. Not. Roy. Astron. Soc.*, 472, 1915
- Cohen A., Fialkov A., Barkana R., Monsalve R. A., 2020, *Monthly Notices of the Royal Astronomical Society*, 495, 4845
- D'Amico G., Panci P., Strumia A., 2018, *Phys. Rev. Lett.*, 121, 011103
- DeBoer D. R., et al., 2017, *Publ. Astron. Soc. Pac.*, 129, 045001
- Dowell J., Taylor G. B., 2018, *Astrophys. J. Lett.*, 858, L9
- Feng C., Holder G., 2018, *Astrophys. J. Lett.*, 858, L17
- Fialkov A., Barkana R., 2019, *Mon. Not. Roy. Astron. Soc.*, 486, 1763
- Fialkov A., Barkana R., Pinhas A., Visbal E., 2014, *Mon. Not. Roy. Astron. Soc.*, 437, 36
- Fialkov A., Barkana R., Cohen A., 2015, *Phys. Rev. Lett.*, 114, 101303
- Fialkov A., Barkana R., Cohen A., 2018, *Phys. Rev. Lett.*, 121, 011101
- Field G. B., 1959, *ApJ*, 129, 536
- Fixsen D. J., et al., 2011, *Astrophys. J.*, 734, 5
- Fraser S., et al., 2018, *Phys. Lett. B*, 785, 159
- Furlanetto S., Pritchard J. R., 2006, *Mon. Not. Roy. Astron. Soc.*, 372, 1093
- Furlanetto S. R., Oh S. P., Pierpaoli E., 2006, *Phys. Rev. D*, 74, 103502
- Gillet N., Mesinger A., Greig B., Liu A., Ucci G., 2019, *Mon. Not. Roy. Astron. Soc.*, 484, 282
- Harker G., 2015, *Mon. Not. Roy. Astron. Soc.*, 449, L21
- Harker G. J. A., Mirocha J., Burns J. O., Pritchard J. R., 2016, *Mon. Not. Roy. Astron. Soc.*, 455, 3829
- Harris C. R., et al., 2020, *Nature*, 585, 357–362
- Hassan S., Liu A., Kohn S., La Plante P., 2019, *Mon. Not. Roy. Astron. Soc.*, 483, 2524
- Hirata C. M., 2006, *Mon. Not. Roy. Astron. Soc.*, 367, 259
- Howson T. L., Scaffidi A., 2021, Introducing NatPy, a simple and convenient Python module for dealing with natural units ([arXiv:2108.07173](https://arxiv.org/abs/2108.07173))
- Hunter J. D., 2007, Computing in science & engineering, 9, 90
- Jennings W. D., Watkinson C. A., Abdalla F. B., McEwen J. D., 2019, *Mon. Not. Roy. Astron. Soc.*, 483, 2907
- Kingma D. P., Ba J., 2014, in 3rd International Conference for Learning Representations, San Diego, 2015. ([arXiv:1412.6980](https://arxiv.org/abs/1412.6980))
- Kovetz E. D., Poulin V., Gluscevic V., Boddy K. K., Barkana R., Kamionkowski M., 2018, *Phys. Rev. D*, 98, 103529
- Levkov D. G., Panin A. G., Tkachev I. I., 2020, *Phys. Rev. D*, 102, 023501
- McKinney W., et al., 2010, in Proceedings of the 9th Python in Science Conference. pp 51–56
- Mebane R. H., Mirocha J., Furlanetto S. R., 2020, *Mon. Not. Roy. Astron. Soc.*, 493, 1217
- Mesinger A., Furlanetto S., 2007, *Astrophys. J.*, 669, 663
- Mesinger A., Furlanetto S., Cen R., 2011, *Mon. Not. Roy. Astron. Soc.*, 411, 955
- Mirocha J., Harker G. J. A., Burns J. O., 2013, *Astrophys. J.*, 777, 118
- Mirocha J., Harker G. J. A., Burns J. O., 2015, *Astrophys. J.*, 813, 11
- Mitridate A., Podo A., 2018, *JCAP*, 05, 069
- Mittal S., Kulkarni G., 2022, *Mon. Not. Roy. Astron. Soc.*, 510, 4992
- Mondal R., et al., 2020, *Mon. Not. Roy. Astron. Soc.*, 498, 4178
- Morales M. F., 2005, *Astrophys. J.*, 619, 678
- Morales M. F., Wyithe J. S. B., 2010, *Ann. Rev. Astron. Astrophys.*, 48, 127
- Moroi T., Nakayama K., Tang Y., 2018, *Phys. Lett. B*, 783, 301
- Natwariya P. K., 2021, *Eur. Phys. J. C*, 81, 394
- Natwariya P. K., Bhatt J. R., 2020, *Mon. Not. Roy. Astron. Soc.*, 497, L35
- Natwariya P. K., Nayak A. C., 2022, *Phys. Lett. B*, 827, 136955
- Natwariya P. K., Nayak A. C., Srivastava T., 2021, *Mon. Not. Roy. Astron. Soc.*, 510, 4236
- Olvera J. d. D. R., Gómez-Vargas I., Vázquez J. A., 2022, *Universe*, 8, 120
- Paszke A., et al., 2019, in , Advances in Neural Information Processing Systems 32. Curran Associates, Inc., pp 8024–8035, <https://papers.neurips.cc/paper/9015-pytorch-an-imperative-style-high-performance-deep-learning-1.pdf>
- Patra N., Subrahmanyam R., Raghunathan A., Shankar N. U., 2013, *Exper. Astron.*, 36, 319
- Pedregosa F., et al., 2011, Journal of Machine Learning Research, 12, 2825
- Peebles P. J. E., 1968, *Astrophys. J.*, 153, 1
- Pospelov M., Pradler J., Ruderman J. T., Urbano A., 2018, *Phys. Rev. Lett.*, 121, 031103
- Price-Whelan A. M., et al., 2018, The Astronomical Journal, 156, 123

- Pritchard J. R., Loeb A., 2010, *Phys. Rev. D*, 82, 023006
- Pritchard J. R., Loeb A., 2012, *Rept. Prog. Phys.*, 75, 086901
- Reis I., Fialkov A., Barkana R., 2020, *Mon. Not. Roy. Astron. Soc.*, 499, 5993
- Saha A. K., Laha R., 2022, *Phys. Rev. D*, 105, 103026
- Schmit C. J., Pritchard J. R., 2018, *Mon. Not. Roy. Astron. Soc.*, 475, 1213
- Seager S., Sasselov D. D., Scott D., 1999, *Astrophys. J. Lett.*, 523, L1
- Seager S., Sasselov D. D., Scott D., 2000, *Astrophys. J. Suppl.*, 128, 407
- Shang W., Sohn K., Almeida D., Lee H., 2016, Understanding and Improving Convolutional Neural Networks via Concatenated Rectified Linear Units ([arXiv:1603.05201](https://arxiv.org/abs/1603.05201))
- Shimabukuro H., Semelin B., 2017, *Mon. Not. Roy. Astron. Soc.*, 468, 3869
- Singal J., et al., 2018, *Publ. Astron. Soc. Pac.*, 130, 036001
- Singh S., et al., 2017, *Astrophys. J. Lett.*, 845, L12
- Singh S., et al., 2022, *Nature Astron.*, 6, 607
- Slatyer T. R., Wu C.-L., 2018, *Phys. Rev. D*, 98, 023013
- Tung J. H., Salamo X. M., Chan F. T., 1984, *Phys. Rev. A*, 30, 1175
- Venumadhav T., Dai L., Kaurov A., Zaldarriaga M., 2018, *Phys. Rev. D*, 98, 103513
- Virtanen P., et al., 2020, *Nature Methods*, 17, 261
- Voytek T. C., Natarajan A., Jáuregui García J. M., Peterson J. B., López-Cruz O., 2014, *Astrophys. J. Lett.*, 782, L9
- Waskom M. L., 2021, *Journal of Open Source Software*, 6, 3021
- Wouthuysen S. A., 1952, *AJ*, 57, 31
- Yang Y., 2018, *Phys. Rev. D*, 98, 103503
- de Lera Acedo E., et al., 2022, *Nature Astron.*, 6, 998

This paper has been typeset from a  $\text{\LaTeX}$  file prepared by the author.